




Multitemporal Mosaicing for Sentinel-3/FLEX Derived Level-2 Product Composites

Damian Ibañez, Ruben Fernandez-Beltran , Senior Member, IEEE, José Martínez Sotoca, Ramón A. Mollineda, José Moreno , Senior Member, IEEE, and Filiberto Pla 

Abstract—The increasing availability of remote sensing data raises important challenges in terms of operational data provision and spatial coverage for conducting global studies and analyses. In this regard, existing multitemporal mosaicing techniques are generally limited to producing spectral image composites without considering the particular features of higher-level biophysical and other derived products, such as those provided by the Sentinel-3 (S3) and Fluorescence Explorer (FLEX) tandem missions. To relieve these limitations, this article proposes a novel multitemporal mosaicing algorithm specially designed for operational S3-derived products and also studies its applicability within the FLEX mission context. Specifically, we design a new operational methodology to automatically produce multitemporal mosaics from derived S3/FLEX products with the objective of facilitating the automatic processing of high-level data products, where weekly, monthly, seasonal, or annual biophysical mosaics can be generated by means of four processes proposed in this work: 1) operational data acquisition; 2) spatial mosaicing and rearrangement; 3) temporal compositing; and 4) confidence measures. The experimental part of the work tests the consistency of the proposed framework over different S3 product collections while showing its advantages with respect to other standard mosaicing alternatives. The source codes of this work will be made available for reproducible research.

Index Terms—Fluorescence explorer (FLEX), mosaicing, open-access data, product composites, Sentinel-3 (S3), time series.

NOMENCLATURE

AVHRR	Advanced Very High Resolution Radiometer.
EO	Earth Observation.
ESA	European Space Agency.
ETM+	Enhanced Thematic Mapper Plus.
EU	European Union.
FAPAR	Fraction of Absorbed Photosynthetically Active Radiation.
FLEX	Fluorescence Explorer.
FLORIS	Fluorescence Imaging Spectrometer.
GeoJSON	Geo-JavaScript Notation.

L1	Level-1.
L2	Level-2.
LC-CCI	Land Cover Climate Change Initiative.
LEDAPS	Landsat Eco-system Disturbance Adaptive Processing System.
LQSF	Land Quality and Science Flag.
LULC	Land use/land cover.
MODIS	Moderate Resolution Imaging Spectroradiometer.
NDVI	Normalized Difference Vegetation Index.
NIR	Near-infrared.
OGVI	OLCI Global Vegetation Index.
OLCI	Ocean and Land Color Instrument.
OTCI	OLCI Terrestrial Chlorophyll Index.
PDGS	Payload Data Ground Segment.
ROI	Region of interest.
RS	Remote sensing.
S2	Sentinel-2.
S2GM	S2 Global Mosaics.
S3	Sentinel-3.
SLSTR	Sea and Land Surface Temperature Radiometer.
SNAP	Sentinel Application Platform.
STC-S2	Short-Term Composite for S2.
STC-S3	Short-Term Composite for S3.
TM	Thematic mapper.
TOA	Top of atmosphere.
UTM	Universal Transverse Mercator.
WELD	Web-Enabled Landsat Data.
WGS84	World Geodetic System 1984.

I. INTRODUCTION

NOWADAYS, the unprecedented availability of the Copernicus open access data provides widespread opportunities to deal with current and future challenges as well as many important societal needs [1]. For instance, fine-grained land cover mapping [2]–[6], natural hazards discovery [7], [8], as well as environmental management and analysis [9]–[11] are some practical RS applications, where the open availability of the Copernicus data plays a fundamental role. The Copernicus program [12] is one of the most important EO programs, which aims at providing global monitoring information from space useful for environmental and security applications. Specifically, different ESA and EU missions plus several national contributing missions have been planned in order to guarantee the operational provision of such RS data [13].

Manuscript received July 2, 2020; revised August 25, 2020; accepted September 8, 2020. Date of publication September 11, 2020; date of current version September 24, 2020. This work was supported in part by the Ministerio de Ciencia, Innovación y Universidades, under Grant RTI2018-098651-B-C54 and in part by Generalitat Valenciana under Grant GV/2020/167. (Corresponding author: Ruben Fernandez-Beltran.)

Damian Ibañez, Ruben Fernandez-Beltran, José Martínez Sotoca, Ramón A. Mollineda, and Filiberto Pla are with the Institute of New Imaging Technologies, Jaume I University, E-12071 Castellón, de la Plana, Spain (e-mail: ibanezd@uji.es; rufernan@uji.es; sotoca@uji.es; mollineda@uji.es; pla@uji.es).

José Moreno is with the Image Processing Laboratory, University of Valencia, E-46980 Valencia, Spain (e-mail: Jose.Moreno@uv.es).

Digital Object Identifier 10.1109/JSTARS.2020.3023593

Among all the program resources, the S3 [14] mission becomes especially adequate for the continuous monitoring of the Earth's surface, since it is focused on the global measurement of the sea and land topography, temperature, and color with a particularly high temporal resolution. The S3 mission comprises a pair of identical satellites: S3A and S3B. They carry four main instruments, including the OLCI as one of the optical sensors, together with the SLSTR. In particular, OLCI captures the Earth's surface using a spatial resolution of 300 m and a total of 21 bands (Oa01–Oa21) in the spectral range between 390 and 1040 nm. With both twin satellites working in conjunction, the PDGS is able to operationally generate and distribute the corresponding OLCI products with a two-day frequency, including processed L1 and derived L2 user products.

Closely related to S3, ESA is currently developing the FLEX [15] mission, which has been designed as an Earth Explorer mission for measuring the terrestrial vegetation fluorescence from space. More specifically, FLEX is a single-satellite mission, which is planned to be launched in 2024, and it will be flying in tandem with S3 for providing (in combination with S3) valuable information about the carbon stored in plants and their role in the global carbon and water cycles. To achieve this goal, FLEX carries the FLORIS that acquires data in the 500–780 nm spectral range, with a sampling step of 0.1 nm and a spatial resolution of 300 m. Thus, FLEX will be exploiting the complementary measurements of S3 to enrich FLORIS L2 products about photosynthesis rates and vegetation stress conditions, which logically provides additional value and interest to S3 operational data [16].

Although OLCI L1 data products contain TOA radiometric measurements, which are radiometrically corrected and calibrated, the L2 processing level provides higher level operational products that are specifically designed for marine and land user applications. In other words, L2 products consist of biophysical and geophysical quantities that represent parameters, which are highly relevant for final users depending on their application field. Precisely, different studies in the literature highlight the advantages of using OLCI L2 products to analyze and monitor several important environmental features. For instance, Kravitz *et al.* [17] show the limitations of using OLCI L1 TOA reflectance products for retrieving small chlorophyll-*a* concentrations in productive inland waters. Kyriliuk and Kratzer [18] present a study that validates multiple derived OLCI L2 in-water products against dedicated *in situ* measurements of the Baltic Sea, obtaining positive results even over near-coastal areas. In [19], Brown *et al.* exploit and validate OLCI L2 terrestrial chlorophyll products of large agricultural areas using synergetic intersensor data. Kokhanovsky *et al.* [20] derive important optical and microphysical properties of snow using the OLCI instrument. Zhang *et al.* [21] study the potential of different OLCI land products for estimating the gross primary productivity across several biomes. The authors also provide interesting insights for their combination with FLEX. Analogously, Lyu *et al.* [22] develop a phytoplankton carbon concentration estimator based on OLCI L2 data in order to investigate the carbon cycle and the global warming effect.

These and other related works mainly point to two key ideas: the great potential of derived OLCI L2 data and the special relevance of generating extensive products to conduct complete and worldwide analyses. The high utility of OLCI L2 products has been widely proven in many research works, including the aforementioned ones and the own S3 mission description [14], that advocate the use of such data in many important applications. However, the part of generating global derived products from OLCI L2 still remains unclear in the RS literature. On the one hand, the spatial coverage of individual S3 products is limited by the PDGS processing chain, which constrains the maximum size of the interest areas in order to ease the online data dissemination [23]. On the other hand, the operational availability of S3 data is often affected by cloud and atmospheric effects, which may logically cause important information gaps when studying those affected areas. In this regard, such limitations on the spatial extension and data availability could be relieved by means of mosaicing and compositing techniques [24].

In general, RS image mosaicing and compositing refer to those algorithmic tools aimed at constructing a full RS scene by aligning partially overlapped multitemporal images. Although the term mosaicing has a classical connotation of spatially scene enlarging, the name compositing accentuates the temporal component, where multiple overlapped images are used to remove data anomalies. In practice, both concepts often work together as multitemporal mosaicing, since the spatial extension and the data availability of the resulting composites are normally equally important in RS [25]. Since the first RS composite method was introduced [26] and evaluated [27] for the AVHRR, different sensor-dependant approaches have been successfully developed in the literature. For instance, Huete *et al.* [28] present a composite technique, based on the NDVI, for the MODIS. In [29], Roy *et al.* present the WELD, which is a multitemporal mosaicing algorithm for Landsat images that selects those reflectance values with minimum clouds, snow, or other type of perturbations. Potapov *et al.* [30] also develop a method especially designed for Landsat, which takes advantage of an initial land cover classification to select the output reflectance according to the NIR band. Additionally, the work presented in [31] studies the feasibility of combining Landsat 5 TM and Landsat 7 ETM+ data to improve the global acquisition coverage. Within the context of Sentinel missions, it is also possible to find a few relevant works. For instance, the Sen2Three algorithm [32] is able to generate corrected spatiotemporal S2 products by selecting the corresponding output composite values using different criteria, e.g., acquisition dates, average aerosol, and solar zenith angle, among others. Similarly, the S2GM [33] approach is also able to produce S2 multitemporal mosaics of reflectance products but in this case using a variation of the WELD algorithm.

Although the utility of mosaicing and compositing techniques for long-term and large-area Earth monitoring has been widely proved using certain types of RS optical data, e.g., Landsat [29] and S2 [33], these technologies have not yet been developed in the context of producing global mosaics of multitemporal OLCI L2 products and the tandem S3/FLEX mission. As was previously mentioned, the use of derived products from OLCI

L2 can provide competitive advantages with respect to low-level reflectance data [14], and it can be highly beneficial in other complementary missions. Note that the higher the processing level, the more adapted the data to the final application domain and hence the simpler their semantic understanding for users. As a result, generating global multitemporal maps of derived products from OLCI L2 instead of reflectance images can be very advantageous, since the nature of these high-level data can be taken into account within the mosaicing process. However, the existing methods are focused on other sensors, and they only deal with the problem from a reflectance-based perspective, which eventually constrains the use of such methods to a higher data processing level.

With all these considerations in mind, this article proposes a novel multitemporal mosaicing algorithm to derive extensive geophysical and biophysical composited mosaics from operational OLCI L2 products. Unlike other methods available in the literature, the proposed approach has been specially designed for the OLCI sensor and its product specifications in order to deal with the higher-level nature of the L2 products provided by the PDGS unit. In more detail, this work has a twofold objective. On the one hand, we intend to highlight the advantages of generating multitemporal OLCI L2 mosaics and how these novel data can help the operational provision of enhanced data products in the context of Sentinel and other Earth Explorer missions like FLEX. On the other hand, we design and release a new operational methodology to automatically produce such multitemporal mosaics from the existing S3 data production chain. That is, the proposed approach takes as input an ROI and a particular temporal period from the Copernicus data dissemination service and it generates as output the corresponding multitemporal L2 mosaic in an unsupervised fashion. The defined methodology pursues to facilitate the automatic data processing regardless of the sensing and ingestion dates of the products in order to provide near-real-time data processing, where the composited mosaics are updated, without human intervention, shortly after the OLCI data are available. In this way, weekly, monthly, seasonal, or annual mosaics of different regions of interest can be easily generated to capture relevant geophysical and biophysical variations on the Earth surface over time. In brief, the main contributions of this work can be summarized as follows.

- 1) We release a new framework to produce, without human intervention, multitemporal OLCI L2 mosaics in order to study worldwide geophysical and biophysical variations on the Earth surface over time.
- 2) We develop a new multitemporal compositing algorithm for derived OLCI L2 data, which considers the nature of the corresponding products to produce more informative results. Besides, we also analyze the proposed approach applicability to the S3/FLEX tandem mission.
- 3) We build several large-scale multitemporal OLCI L2 composite mosaics of Europe to validate the performance of the proposed framework. The codes related to this work will be available for reproducible research.¹

¹[Online]. Available: <https://github.com/rufernan/S3L2Mosaicing>

The rest of this article is organized as follows. Section II reviews some of the most important methods on RS image mosaicing and compositing. Section III presents the proposed framework while also detailing its constituent parts and validation. In Section III-E, we study the adaptation possibilities of the presented scheme to the FLEX mission environment. Section IV contains the experimental part of the work where several OLCI worldwide biophysical composites are obtained, validated, and compared. Finally, Section V concludes this work and provides some interesting future research lines.

II. RELATED WORK

This work is particularly focused on generating multitemporal mosaics from derived OLCI L2 data products. Several multitemporal mosaicing algorithms have been developed for other satellites or data, and this section reviews some of the most relevant approaches. For Landsat images, the WELD algorithm [29] was designed to select land pixels with minimum cloud, snow, or other type of atmospheric contamination in Landsat products. WELD is based on the LEDAPS [34]. It uses monthly, seasonal, and annual sets of images to generate consistent land mosaic geophysical and biophysical products for detailed regional assessments of land cover dynamics and to study Earth system functioning. Specifically, the considered decision tree utilizes the NDVI, brightness temperature, maximum apparent surface temperature, minimum scan angle, maximum difference in red, and NIR reflectance as well as combinations of these to compare two pixels and obtain the best representative. The following equation shows the expression corresponding to the NDVI:

$$\text{NDVI} = \frac{(\rho_{\text{nir}} - \rho_{\text{red}})}{(\rho_{\text{nir}} + \rho_{\text{red}})} \quad (1)$$

where ρ_{nir} represents the reflectance of the NIR band and ρ_{red} represents the reflectance of the red band. The main drawback of the WELD algorithm is that it is not very robust if the spectrum does not satisfy the quality control of the classification segment.

There are more statistical methods, such as the median NIR composite method, which has been used for different regional studies using Landsat data in Russia [30] and in Democratic Republic of the Congo [35]. In detail, this method is an evolution of the approach presented in [36], which uses filtered data with a classification of water, cloud, shadow, and other similar classes, giving a set of image dates forming a data pool from which the best observation date per composite is selected. From the same classification scheme, the median NIR value is chosen as the best pixel value. The median NIR method has shown advantages for temporal time-series coarse spatial resolution data compositing compared to the heritage maximum NDVI approach. Besides, it was proved to produce the least noisy outputs over forested areas.

A different approach was proposed by Flood [37] using the medoid function. The medoid is the representative object of a dataset, whose average dissimilarity to all the objects in the dataset is at a minimum [38]. The medoid applied to reflectance [37] is estimated by calculating the distance between all the different reflectance pixel values in each band and minimizes

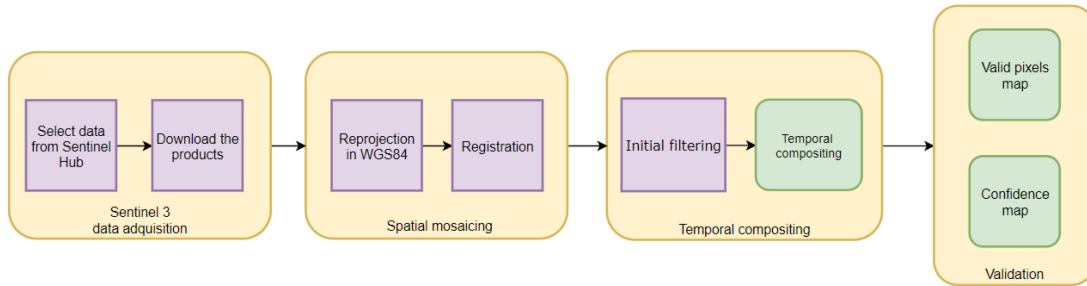


Fig. 1. Proposed multitemporal mosaicing framework for derived OLCI L2 products.

its sum. It appears to be better than the median at producing imagery that are representative of a time period. This method was also applied to Landsat TM/ETM+ imagery to create seasonal reflectance images, and an analysis of the seasonal reflectance values suggests this composite as a better representative than the maximum NDVI seasonal composite. The medoid function can be expressed as follows:

$$\text{Medoid}(\mathbf{x}) = \underset{x_i \in \mathbf{x}}{\operatorname{argmin}} \sum_{x_j \in \mathbf{x}} \|x_j - x_i\| \quad (2)$$

where it is defined as the point x_i in the set \mathbf{x} that minimizes the sum of the distances between this point and all the other points x_j in the set.

Regarding Sentinel missions, in the case of S2, the Sen2Three algorithm [32] generates synthetic atmospherically corrected S2 L2 spatiotemporal products as they are generated by Sen2Cor atmospheric correction software [39]. This method changes the pixels that have been considered contaminated from others of a time series following three criteria: the newer acquisition date is ranked higher, a ranking according to the sum of good pixels, and a ranking according to the average aerosol optical thickness or the average of the solar zenith angle. Another compositing approach was done by the S2GM [33]. It was designed to generate mosaics of the surface reflectance L2 products from S2. This algorithm takes as input a time series and, pixel by pixel, it uses two different strategies depending on the number of valid samples: 1) the medoid algorithm and 2) a variation of the WELD algorithm adapted for S2 products with a land cover classification named the STC-S2. In more detail, S2GM performs a spatial resampling using the nearest neighbor method for different resolution observations and makes the spatial mosaicing using the SNAP toolbox mosaicing approach [40].

III. PROPOSED FRAMEWORK

This section presents the methodological part of the work, which has been designed to generate multitemporal OLCI mosaics according to four sequential modules (see Fig. 1): 1) the operational data acquisition, where the original data are obtained and downloaded from the Sentinel-Hub (see Section III-A); 2) the spatial mosaicing and rearrangement of the downloaded products, performing a reprojection to WGS84 coordinates and a spatial registration process (see Section III-B); 3) the temporal compositing after filtering the data (see Section III-C); and 4) a

final validation of the multitemporal product mosaics showing the valid number of pixels and their corresponding confidence levels (see Section III-D). Additionally, Section III-E provides some remarks to adapt the proposed framework to other relevant missions, such as FLEX.

A. Operational Data Acquisition

The first step of the proposed framework aims at collecting the corresponding OLCI L2 products of interest for generating the output multitemporal mosaic. It is important to highlight that the task of generating global composites usually demands dealing with vast amounts of operational RS data [41], which logically raises some technical challenges (in terms of data acquisition, storage, and automatization) that this initial step tries to cope with. More specifically, we make use of the available Copernicus data provision services in the following way. First, we define an ROI R based on a closed polygonal shape of geocoordinates using the GeoJSON format. Besides, we also consider a temporal interval T of the multitemporal mosaic as input for the data acquisition process. Then, given an ROI R and a temporal interval T , we build the corresponding query for obtaining the list of suited OLCI L2 products from the Copernicus open access hub [42]. Once the list of relevant product identifiers has been retrieved, we iterate (in a batch processing mode) to automatically download the corresponding operational products (together with their metadata information) in a compressed format.

B. Spatial Mosaicing for OLCI L2 Products

The second step consists in mosaicing all the downloaded products in a global spatiotemporal grid taking into account the possible geolocation deviations among operational data products. Let X_r^t be a derived L2 product covering the region r of the Earth surface at the time instant t , where X_r^t pixels are geospatially located in terms of UTM coordinates. In order to simplify and make a more accurate geospatial registration of multiple overlapped product images X_r^t for a region r and different times t , pixels are projected to WGS84 coordinates using the SNAP toolbox [40]. Thus, transformed pixels are the same size in this coordinate systems, making them easier to fit and overlap into the mosaic structure. Since this process might introduce small location errors, a resampling process will still be necessary.

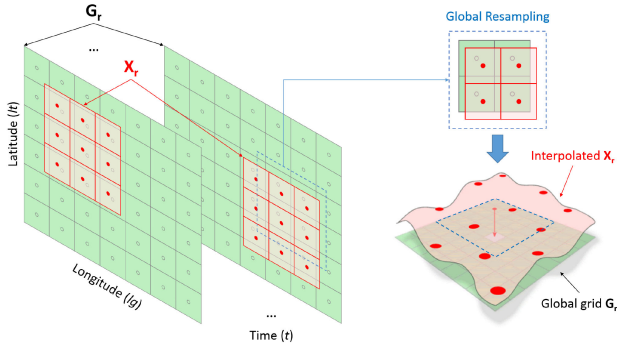


Fig. 2. Product interpolation to generate the global spatiotemporal 3-D grid $G_r(lt, lg, t)$.

Accordingly, a spatiotemporal 3-D grid is built from a number of operational L2 product images $G_r(lt, lg, t)$ representing the region r and time instants close enough to produce a useful mosaic. Grid axes are defined into a range of latitude lt (height), longitude lg (width), and time t (depth) interval that allow all the images X_r^t to be spatially registered into this grid, while the spatial resolution is set to 300 m as in the S3 OLCI sensor. Since grid coordinates do not generally agree with those calculated for each initial product X_r^t when they are transformed into the grid G spatial coordinates, an interpolation process is performed using a kernel to estimate the product values expected in the grid coordinates as shown in Fig. 2. The spatially transformed product data of initial X_r^t are then stacked in the 3-D grid temporal layer t , that is, $G_r(lt, lg, t) = L(X_r^t)$, where L is the latitude–longitude transformation from UTM coordinates.

C. Temporal Compositing for OLCI L2 Products

Once all the products of interest are represented as an uniform spatiotemporal cube, the third step of the proposed framework pursues to conduct the temporal compositing. Specifically, the compositing of the temporal data is done by choosing the best pixel value from the set of valid temporal samples depending on several factors: number of valid temporal samples, LULC classification of pixels, nominal value of the product, and other important aspects such as solar zenith angle during acquisition or product value statistical median.

As seen in Section II, previous works mainly perform the mosaicing of L2 reflectance bands of S2 products or Landsat products. However, none of these methods can be directly used to create mosaics of other operational derived L2 products. These previous works showed that the medoid and median algorithms are the most adequate when integrating time-series values, but a minimum number of valid pixels is needed to get satisfactory results. Because the aim of this work is mosaicing biophysical and other derived L2 products, different from spectral reflectance band product images, the lack of temporal observations may be particularly critical in this situation. Note that the considered input data correspond to univariate quantities that represent high-level biophysical and geophysical parameters; then, the robustness of the medoid algorithm against the presence of outliers is aligned with the univariate median [37].

TABLE I
CONDITIONS IN THE FILTERING

Priority	Criteria
1	The pixel is classified as LAND, WATER or SNOW-ICE
2	The pixel value in the product is a valid finite number
3	The solar zenith value of the product is less than 70.0°

Thus, in this work, we propose the median of the observations when there is a minimum number of valid time samples for a pixel $G_r(lt, lg, t)$. In case there are not enough valid samples for a pixel, following S2GM [33] and WELD [29] methods, a decision tree is used. The decision tree designed considers S3 OLCI L2 classification information as well as the index of the target product, and it consists in a variation of the STC-S2 algorithm used for S2 L2 products.

Once the spatiotemporal grid $G_r(lt, lg, t)$ is built by means of the described geospatial registration process, the proposed mosaicing algorithm for S3 OLCI products can be divided into two main modules: a previous filtering of the $G_r(lt, lg, t)$ data (see Section III-C1) and the temporal resampling and compositing based on the median and the newly defined STC-S3 (see Section III-C2).

1) *Filtering*: Given the temporal 3-D grid $G_r(lt, lg, t)$, a preliminary filtering is needed to consider only valid temporal pixel values. Within the available S3 OLCI L2 products, there is an LQSF product. This product provides a classification of every pixel in different classes, including water, land, clouds, and snow. This classification is done by taking into account indices, band ratios, TOA spectral reflectance, OGVI, and OTCI spectral tests [43]. There are 25 classes in total, having also flags for pixel quality, possible fails in readings, and saturation. There is another L2 product concerning ocean quality and science flags, but since the experimentation was focused on land products, this classification was not used.

It is worth noting that the LQSF product does not provide classes for vegetation or soil. They are all included in the land class because the OLCI sensor was initially oriented to water characterization and monitoring. Nevertheless, different flags in the LQSF product can provide additional information about vegetation indices. This is the case of the OGVI flag, which stands for the OGVI provided by S3. This index is calculated from the FAPAR estimation using the algorithm provided by the LQSF product.

In order to illustrate how the mosaicing and temporal compositing algorithm works, the S3 OTCI index has been chosen as biophysical L2 product for mosaicing. OTCI estimates chlorophyll in S3, and it is defined as follows:

$$\text{OTCI} = \frac{(\text{Oa12} - \text{Oa10})}{(\text{Oa11} - \text{Oa10})} \quad (3)$$

where Oa12, Oa11, and Oa10 are the reflectance in bands centered at 753, 709, and 681 nm, respectively, of the OLCI sensor. A pixel value is considered valid when the three different conditions expressed in Table I are satisfied. High solar zenith (values higher than 70.0°) are not taken into account as these data can be physically unrealistic. This was concluded in [44]

for the MODIS accuracy, and it can be applied to S3 as well. In addition, all the product values that are not valid or finite are filtered. Those pixels not classified as LAND, WATER, or SNOW-ICE have also been filtered out, as well as those classified as INVALID or any CLOUD pixel class. After the filtering step, the spatial coordinate (lt, lg) gathers together a number of valid temporal values $\{G_r(lt, lg, t); t \in V_t(lt, lg)\}$, where $V_t(lt, lg)$ is the time stamps set linked to (lt, lg) . The resulting data are ready to be used in the compositing phase.

2) *Compositing and Temporal Resampling*: The composition and temporal resampling module integrates the previously filtered pixel values to obtain a representative $C_r(lt, lg)$ for each pixel (lt, lg) from the corresponding temporal set of valid product values $\{G_r(lt, lg, t); t \in V_t(lt, lg)\}$. After filtering, different amounts of valid samples per pixel are expected. Let $N_t(lt, lg) = |V_t(lt, lg)|$ be the number of valid temporal samples in the temporal grid. Depending on this number of valid observations, a specific strategy is used.

When sufficient valid observations are available, the representative value $C_r(lt, lg)$ is obtained as the median of the set $\{G_r(lt, lg, t); t \in V_t(lt, lg)\}$. The median is a robust estimator when dealing with a small proportion of outliers in enough data samples. However, the median might provide a biased estimate when outliers affect a small amount of data. This is why median is only used when the available temporal samples is larger than a certain threshold th_m . If the number of temporal samples is larger than such threshold, the median is used; otherwise, an adaptation of the STC for S3 algorithm $STC_S3(lt, lg)$ here proposed is used. In this work, the threshold value has been set to 4 in order to have the median working properly with a minimum number of samples (as in [33]), thus reducing the probability that outliers affect the final estimate. With regard to the STC method, even with a few samples, it is able to obtain useful information through the pixel identification auxiliary criteria. These methods are considered simple and appropriate enough to perform automated large mosaic composition of S3 operational L2 products. In summary, the compositing algorithm can be formulated as

$$C_r(lt, lg) = \begin{cases} \text{if } N_t(lt, lg) > th_m, & \text{then } M_r(lt, lg) \\ \text{otherwise} & STC_S3(lt, lg) \end{cases} \quad (4)$$

The proposed adaptation of the STC for S3 is based on the STC-S2 from the S2GM algorithm [33], the WELD algorithm [29], and the LC-CCI WELD for S2 [45]. These algorithms have been proposed to reduce aerosol contamination and residual clouds in time series. In the algorithm adapted for S3 L2 land products, the best pixel from a small set of valid time samples is selected based on a decision tree using the derived product values, pixel classification, and other flags.

The proposed $STC_S3(lt, lg)$ algorithm takes for a given pixel (lt, lg) two out of the valid temporal samples, $G_r(lt, lg, t_1)$ and $G_r(lt, lg, t_2)$, with $t_1, t_2 \in V_t(lt, lg)$, to compare each other. The comparison possibilities of the proposed STC_S3 can be summarized in Algorithm III-C2, where $T(\cdot)$ is the decision tree function shown in Fig 3. Table II also summarizes the decision tree algorithm logic. As in the WELD and the STC-S2 algorithm, each row in the table is a comparison between two valid temporal

Algorithm 1: $STC_S3(lt, lg)$ Algorithm to Select a Temporal Value for Pixel (lt, lg) .

Result: $STC_S3(lt, lg)$
 $G_r^* \leftarrow G_r(lt, lg, t_1); i \leftarrow 2;$
while $i \leq |V_t(lt, lg)|$ **do**
 $G_r^* \leftarrow T(G_r^*, G_r(lt, lg, t_i)); i \leftarrow i + 1;$
end
Return $STC_S3(lt, lg) \leftarrow G_r^*;$

samples in the 3-D grid $G_r(lt, lg, t_1)$ and $G_r(lt, lg, t_2)$, and if this comparison is not met, the next row compositing condition is checked. The process repeats until a condition is met or the last default rule is reached.

According to the LQSF product, S3 pixels can be classified as LAND, WATER, and SNOW_ICE. The other available classes, INVALID and pixels with CLOUD flag, are discarded. Note that vegetation is included in LAND class and further checks using OGVI and OTCI values, which allow us to identify the temporal pixel values related to vegetation. The fundamentals of the decision tree rules are based on the following criteria, depending on the properties of the two temporal pixel samples under comparison.

- 1) Pixels classified as LAND have the highest priority to be selected as they may be vegetation unlike the other possible classifications.
- 2) If pixels are not classified as LAND, then SNOW_ICE and WATER classes have the second and third priority levels, respectively. Note that SNOW_ICE is the second class of pixels likely to be misclassified in LAND areas and WATER is the last option.
- 3) A further check is done by the OGVI in order to increase the probability of a correct characterization of the pixel as vegetation, since vegetation pixels may also be classified as SNOW_ICE, CLOUD, or WATER. This additional check could be avoided in case the objective is to focus on high confidence values for vegetation. In the experiments, it has been applied for the sake of completeness.
- 4) When two temporal values of a pixel belong to the same class, the pixel sample with the maximum OTCI value is selected, that is, the highest value of chlorophyll becomes the estimate for that pixel in the considered time period.
- 5) OTCI values may vary among all temporal valid samples for the same pixel location in a short period of time. Part of the reasons for this behavior may be due to differences in phenology as a result of images in adjacent paths being collected at different times. One way to minimize this effect is trying to select valid temporal values of a pixel in the composite from roughly the same phenological stage, for example, when the leaves are photosynthetically active. An approximate and simpler criterion is choosing the maximum OTCI value, in order to keep the highest recorded photosynthetic activity in the temporal period considered for the composite.

The above described criteria were designed to classify and select pixel values to obtain mosaics and temporal composites

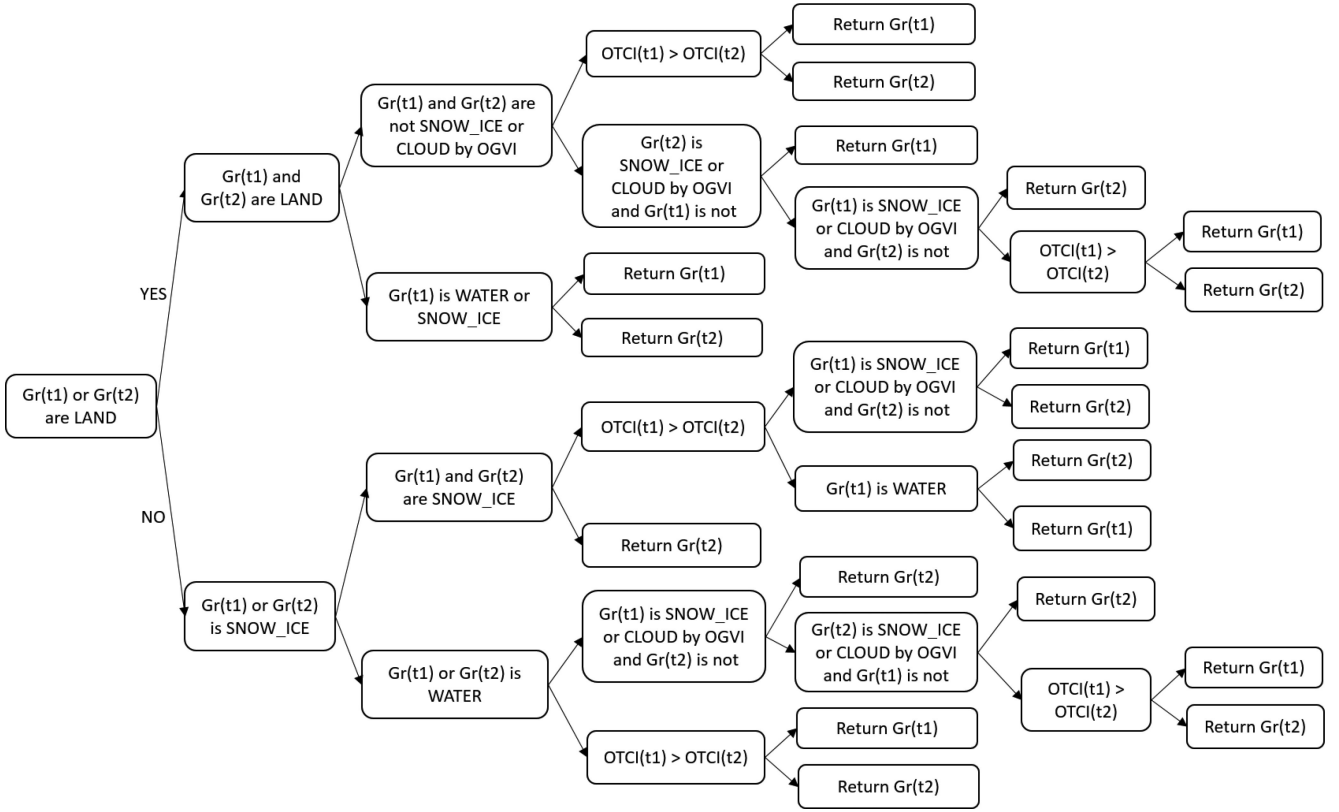


Fig. 3. Decision tree algorithm for function $T(G_r(t_1), G_r(t_2))$ when comparing two valid temporal samples, $G_r(lt, lg, t_1)$ and $G_r(lt, lg, t_2)$, of a pixel (lt, lg) .

TABLE II
COMPOSITING CRITERIA USED IN THE DECISION TREE FUNCTION $T(G_r(t_1), G_r(t_2))$ WHEN COMPARING TWO VALID TEMPORAL SAMPLES, $G_r(lt, lg, t_1)$ AND $G_r(lt, lg, t_2)$, OF A PIXEL (lt, lg) .

Priority	Compositing criteria
1	Both $G_r(t_1)$ and $G_r(t_2)$ are LAND (by LQSF) and none of them are CLOUD or SNOW_ICE (by OGVI): Select the maximum OTCI value
2	$G_r(t_1)$ and $G_r(t_2)$ are LAND (by LQSF) and one of them is CLOUD or SNOW_ICE (by OGVI): Select the OTCI value of the one not classified as CLOUD or SNOW_ICE
3	$G_r(t_1)$ and $G_r(t_2)$ are LAND (by LQSF) and both are CLOUD or SNOW_ICE (by OGVI): Select the maximum OTCI value
4	Either $G_r(t_1)$ or $G_r(t_2)$ is LAND (by LQSF) and the other one is SNOW_ICE or WATER (by LQSF): Select the OTCI value of LAND
5	Both $G_r(t_1)$ and $G_r(t_2)$ are SNOW_ICE (by LQSF): Select the maximum OTCI value
6	Either $G_r(t_1)$ or $G_r(t_2)$ is SNOW_ICE (by LQSF) and the other one is WATER (by LQSF): Select the OTCI value of SNOW_ICE
7	Both $G_r(t_1)$ and $G_r(t_2)$ are WATER (by LQSF) and none of them are WATER (by OGVI): Select the maximum OTCI value
8	$G_r(t_1)$ and $G_r(t_2)$ are WATER (by LQSF) and one of them is WATER (by OGVI): Select the OTCI value of the one classified as WATER by OGVI
9	$G_r(t_1)$ and $G_r(t_2)$ are WATER (by LQSF) and both are WATER (by OGVI): Select the maximum OTCI value

for S3 L2 OTCI products. In case of mosaicing other products, different criteria for the STC algorithm should be defined, for example, for water products such as the Algal Pigment Concentration. Nevertheless, apart from the corresponding criteria of the STC-S3 algorithm for a given product, the rest of the temporal compositing and mosaicing algorithm remains the same.

D. Validation of OLCI Product Mosaics

In order to validate the generated multitemporal OLCI product mosaics, as there is not any ground truth available, two different confidence measures are proposed to assess the quality of the generated mosaic. A simple and quick look to the mosaic confidence values can be provided by a map showing the number

of valid temporal samples in the pixels temporal grid, that is, $N_t(lt, lg)$.

Another straightforward statistics could be the standard deviation of the valid temporal product values for each pixel. However, taking into account that the number of valid observations $N_t(lt, lg)$ is usually small and that they may include outliers, the standard deviation does not appear to be a very reliable measure.

Instead of using the standard deviation $S(\bar{G}_r(lt, lg))$ of the mean $\bar{G}_r(lt, lg)$ as uncertainty measure, if there are at least two values, the standard deviation of the valid observations for each pixel is weighted by the critical value of the Student's t -distribution [46] corresponding to the number of valid observations and a significance level $\alpha = 0.05$. Eventually, the proposed confidence index is expressed as

$$u_A(lt, lg) = e^{-t_{N_t-1;95\%} * S(\bar{G}_r(lt, lg))}. \quad (5)$$

The standard deviation $S(\bar{G}_r(lt, lg))$ is then defined as

$$S(\bar{G}_r(lt, lg)) = \frac{\sqrt{\frac{1}{N_t-1} * \sum_{t=1}^{N_t} (\bar{G}_r(lt, lg) - G_r(lt, lg, t))^2}}{\sqrt{N_t}} \quad (6)$$

And the mean $\bar{G}_r(lt, lg)$ is defined as

$$\bar{G}_r(lt, lg) = \frac{\sum_{t=1}^{N_t} G_r(lt, lg, t)}{N_t}. \quad (7)$$

In summary, the confidence index $u_A(lt, lg)$ of a pixel mosaic value $C_r(lt, lg)$ is defined as the inverse exponential of the t -distribution $t_{n-1;95\%}$ weighted standard deviation $S(\bar{G}_r)$ in order to provide the confidence index in the $[0,1]$ interval. The weight $t_{n-1;95\%}$ increases the confidence proportionally with the number of valid observations (degrees of freedom), due to the smaller associated critical values of the t -distribution. Thus, the proposed $u_A(lt, lg)$ confidence index provides a normalized confidence measure that accounts for both the standard deviation and the number of valid observations.

E. FLEX Adaptation

The algorithm previously proposed has been designed for S3. In order to use it in future works with FLEX L2 derived products, some changes are needed. As S3 and FLEX will fly in tandem following the same orbit with few seconds delay and FLEX will deliver products with the same spatial resolution as S3, 300×300 m per pixel, a geospatial registration between an S3 and a FLEX products has to be done. This geospatial registration could be done as described in Section III-A to build a common 3-D temporal grid from S3 and FLEX simultaneously.

If a FLEX L2 classification pixel product is provided, the decision tree of the STC-S3 presented algorithm will have to be adapted to the available set of classes in FLEX. In any case, the same S3 L2 LQSF product can be used, after geospatial registering the corresponding FLEX and S3 images. Therefore, we can assign the S3 pixel classification to the corresponding FLEX pixel and use the STC-S3 decision tree proposed, as it is already improved for land and vegetation products. The main change in the algorithm would be substituting the OTCI product by the selected FLEX product, such as fluorescence, which is

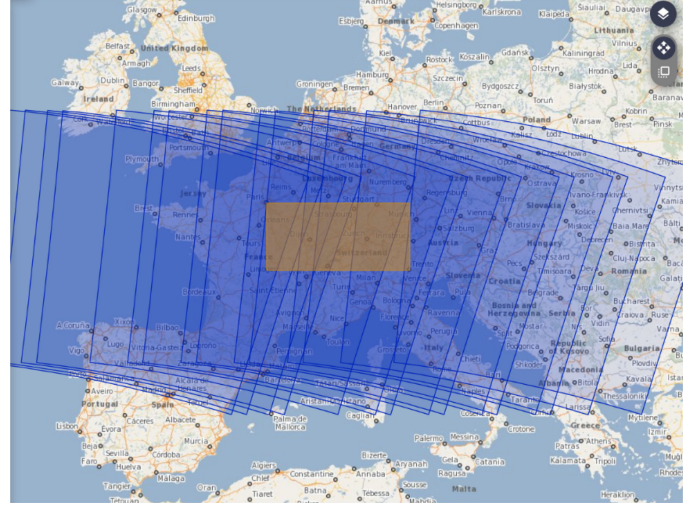


Fig. 4. Data products considered for the Autumn-peak dataset.

the main product that will be provided by FLORIS, the FLEX sensor.

However, this modification would also have additional implications due to the dynamic nature of the fluorescence phenomenon with respect to the chlorophyll content. Although the chlorophyll concentration tends to be stable in short periods of time (hours or even days), the fluorescence is a dynamic biophysical parameter that would require a supplementary model for characterizing the existing intra-day variations. Note that the local solar time along the FLEX/S3 orbit logically affects the fluorescence captured by FLORIS, and hence, it can generate some artificial deviations between different fluorescence products. To address this problem, we highlight the need of developing an empirical model (based on actual FLEX measurements) to characterize how the fluorescence parameter is affected by the orbit acquisition point and the local time. In this way, each individual product could be corrected according to its particular acquisition conditions before performing the spatial mosaicing step (see Section III-B). A similar scheme could also be applied for other available FLEX products.

IV. EXPERIMENTS

This section presents the experimental part of the work, including details of the considered datasets in Section IV-A, the experimental setup in Section IV-B, and the obtained results together with their corresponding validation in Section IV-C.

A. Dataset

In this work, we use different sets of multitemporal OLCI L2 products to produce their corresponding OTCI mosaics. Specifically, we select the region between Paris (France) and Trento (Italy) as ROI. That is, we only consider those operational products that include some part of the rectangular area between the (48.864716, 2.349014) and (46.06787, 11.12108) latitude–longitude coordinates. Given this ROI, we define the following datasets for the experiments.

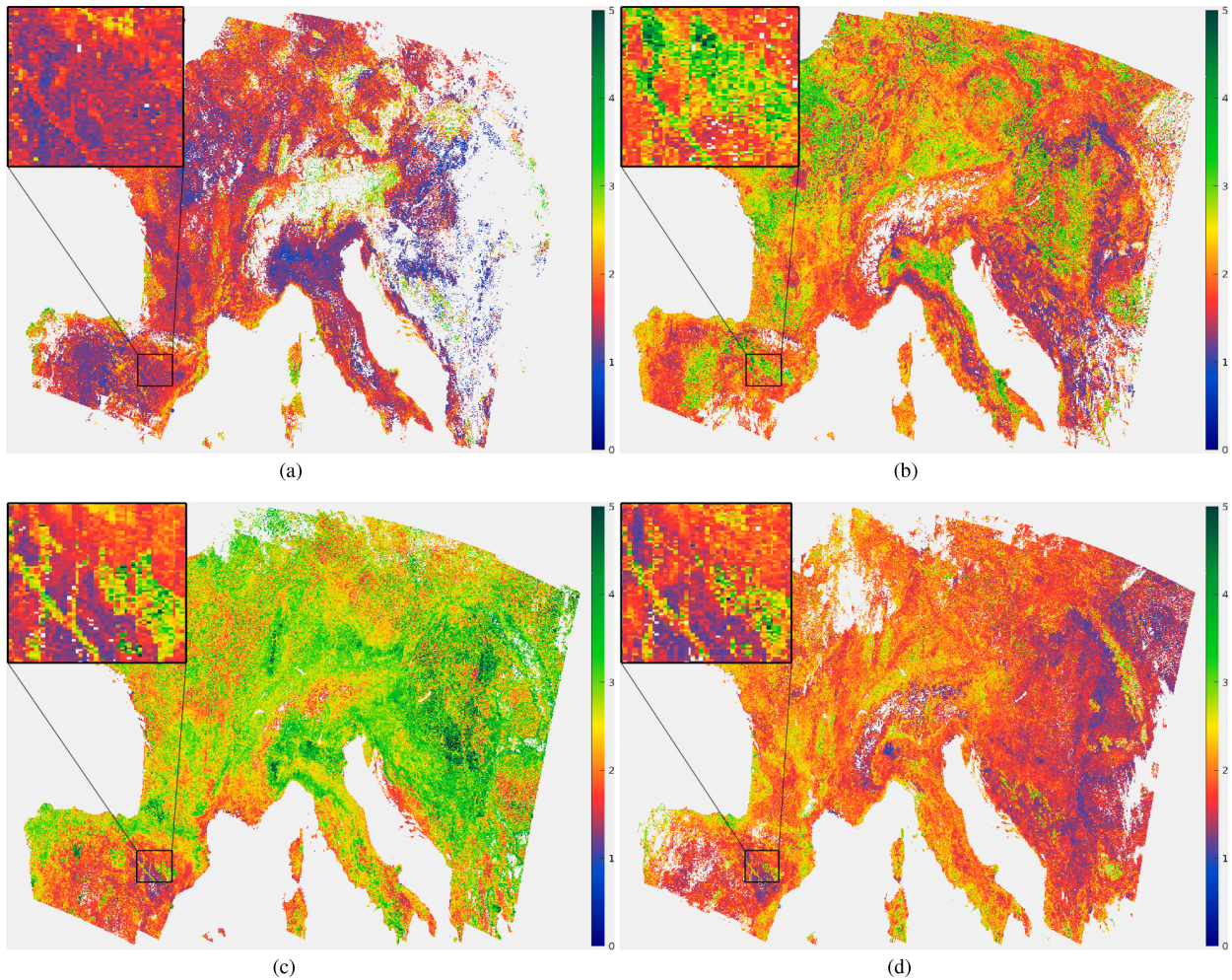


Fig. 5. OTCI mosaics generated by the proposed framework in Experiment 1. Note that the blue to green color scale is used to represent different OTCI values and the gray color expresses unavailable or nonvalid pixels. (a) Winter-peak. (b) Spring-peak. (c) Summer-peak. (d) Autumn-peak.

- 1) *Winter-peak*: From the 15th to the 31st of January 2019 (27 products).
- 2) *Spring-peak*: From the 15th to the 21st of April 2019 (15 products).
- 3) *Summer-peak*: From the 15th to the 21st of July 2019 (15 products).
- 4) *Autumn-peak*: From the 14th to the 20th of October 2019 (15 products).
- 5) *April-1st*: From the 1st to the 7th of April 2019 (16 products).
- 6) *April-2nd*: From the 8th to the 14th of April 2019 (15 products).
- 7) *April-3rd*: From the 15th to the 21st of April 2019 (15 products).
- 8) *April-4th*: From the 22nd to the 30th of April 2019 (17 products).

As an illustrative example, Fig. 4 shows in blue the area of the OLCI L2 products considered for the *Autumn-peak* dataset and the considered ROI in orange. Note that all the datasets include operational products from one week, except *Winter-peak* that covers two weeks due to the high amount of clouds present in Europe during the winter season. These datasets have been

selected to allow analyzing the seasonal evolution of the vegetation in central Europe throughout the generated OTCI mosaics. Since the values of the considered vegetation index are highly variable along time, we additionally consider weekly OTCI mosaics in April. In this case, the third week of April (*April-3rd*) corresponds to the peak of the spring season (*Spring-peak*).

B. Experimental Setup

For each one of the considered datasets, we apply the proposed framework to download the operational products, generate the corresponding OTCI mosaics, and validate the results according to the confidence measure provided in Section III. Although operational OLCI L2 products contain multiple data [23], it is important to note that only OTCI and LQSF product information is used for generating the corresponding multitemporal OTCI mosaics. To better organize the results, we divide the experiments into the following two setups.

- 1) *Experiment 1*: In this experiment, we consider the *Winter-peak*, *Spring-peak*, *Summer-peak*, and *Autumn-peak* datasets in order to conduct an interseason OTCI analysis for the year 2019.

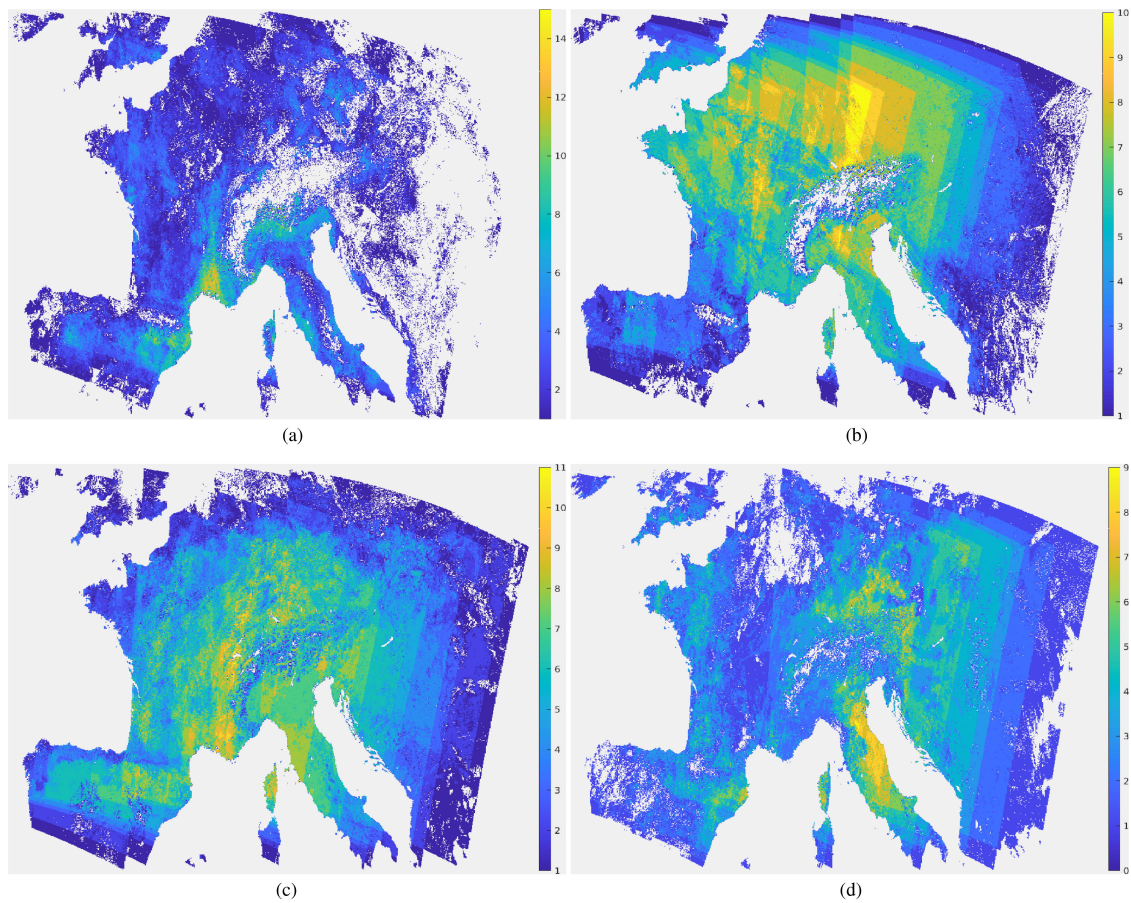


Fig. 6. Valid pixel maps for the OTCI mosaics generated in Experiment 1. Note that the blue to yellow color scale is used to represent valid pixel counts and the gray color expresses unavailable information. (a) Winter-peak. (b) Spring-peak. (c) Summer-peak. (d) Autumn-peak.

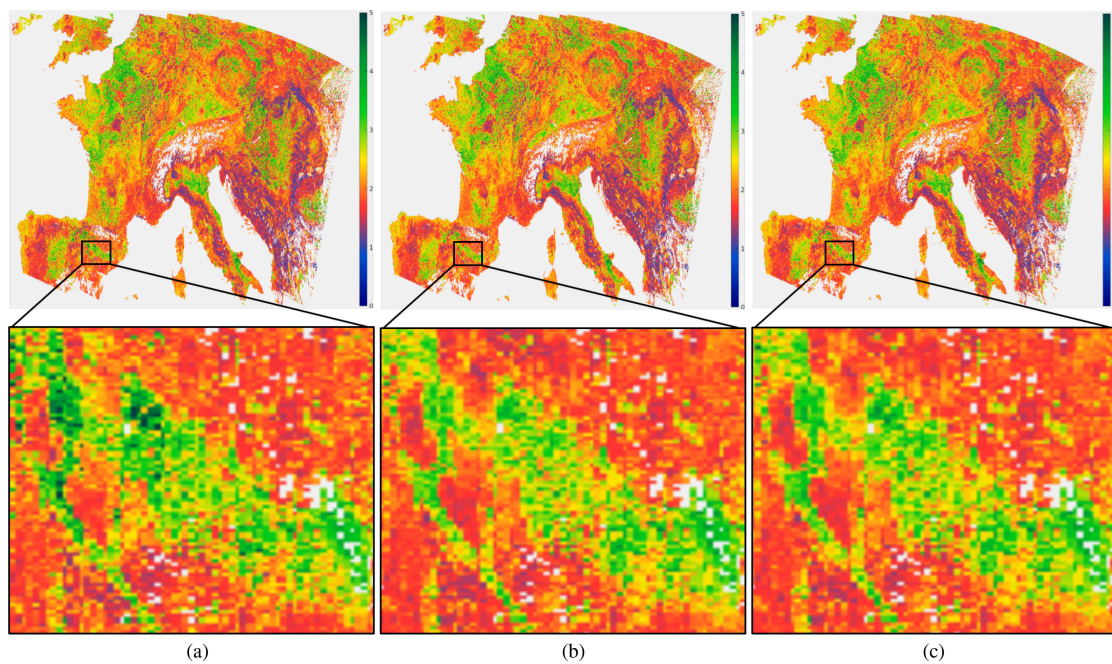


Fig. 7. Qualitative comparison among different OTCI composites for the *Spring-peak* dataset. (a) Proposed. (b) Mean. (c) Median.

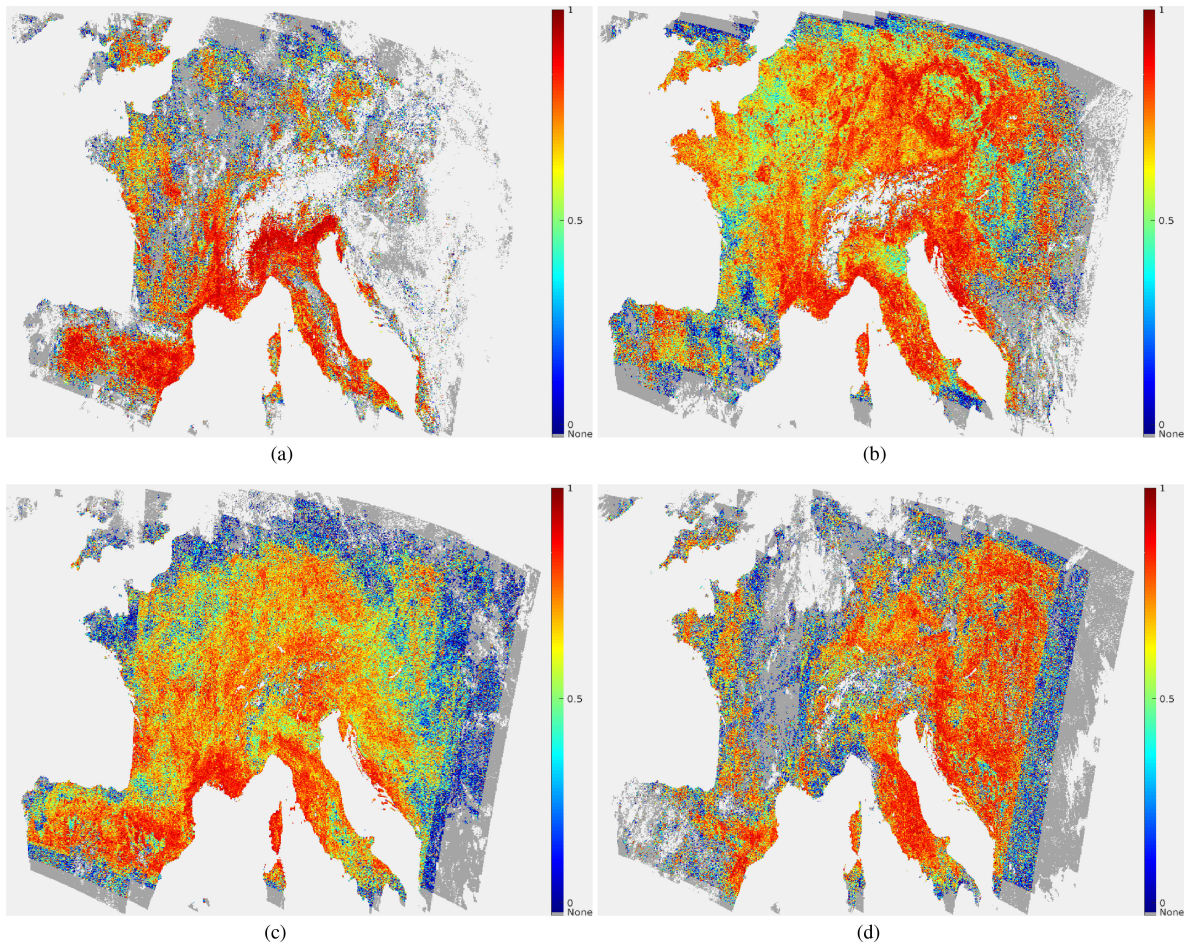


Fig. 8. Confidence maps for the OTCI mosaics generated in Experiment 1. Note that the blue to red color scale is used to represent pixel confidence values and the gray color expresses unavailable information (light gray) or a single valid pixel (dark gray), where the proposed confidence metric is not defined. (a) Winter-peak. (b) Spring-peak. (c) Summer-peak. (d) Autumn-peak.

2) *Experiment 2*: This experiment includes the datasets *April-1st*, *April-2nd*, *April-3rd*, and *April-4th* to study the evolution of the OTCI mosaics along April 2019.

Regarding the software and hardware environments, all the experiments conducted have been built on the top of the Python 3.5.2 and MATLAB 2019a frameworks, and they have been executed on a Ubuntu 16.04 x64 server with 24 Intel(R) Xeon(R) E5-2640 processors with 189-GB RAM. The related codes are available for reproducible research.

C. Results

1) *Experiment 1*: Fig. 5 presents the OTCI mosaics generated by the proposed framework for the *Winter-peak* (a), *Spring-peak* (b), *Summer-peak* (c), and *Autumn-peak* (d) datasets. As it is possible to observe, low OTCI values are represented in blue colors, whereas high OTCI values (indicating a high chlorophyll content) are represented in green. Additionally, unavailable or nonvalid pixel values are displayed in gray color. Note that this color scale is the one officially provided to be used with Sentinel-Hub services,² where reddish colors represent very

low chlorophyll concentrations and greenish colors express high chlorophyll values related to more dense and healthier vegetation. From the obtained mosaics, it is possible to make some important observations. In general, the interseason analysis of the generated European composites reveals that the maximum amount of green vegetation is achieved in the summer season, followed by the spring, autumn, and winter seasons as it is expected according to the considered European region [47]. Nevertheless, some specific areas of interest exhibit a different trend, as it is the case of the detail displayed in Fig. 5 that includes the northern part of the *Aragón* autonomous community in north-east Spain [48]. More specifically, this region contains different natural parks, such as the *Sierra y Cañones de Guara* [49], which are principally made of coniferous trees, such as the *Pinus nigra* and *Pinus sylvestris*, that increase their photosynthetic activity during the peak of the spring season by means of a higher foliar pigment level [50]. Precisely, this increase can be clearly observed in the multitemporal composite generated in Fig. 5(b), which reveals the proposed framework consistency when building mosaics from OLCI-derived products acquired on different dates.

Regarding the data availability, the number of valid temporal observations considered in each mosaic is another relevant

²[Online]. Available: <https://github.com/sentinel-hub/custom-scripts>

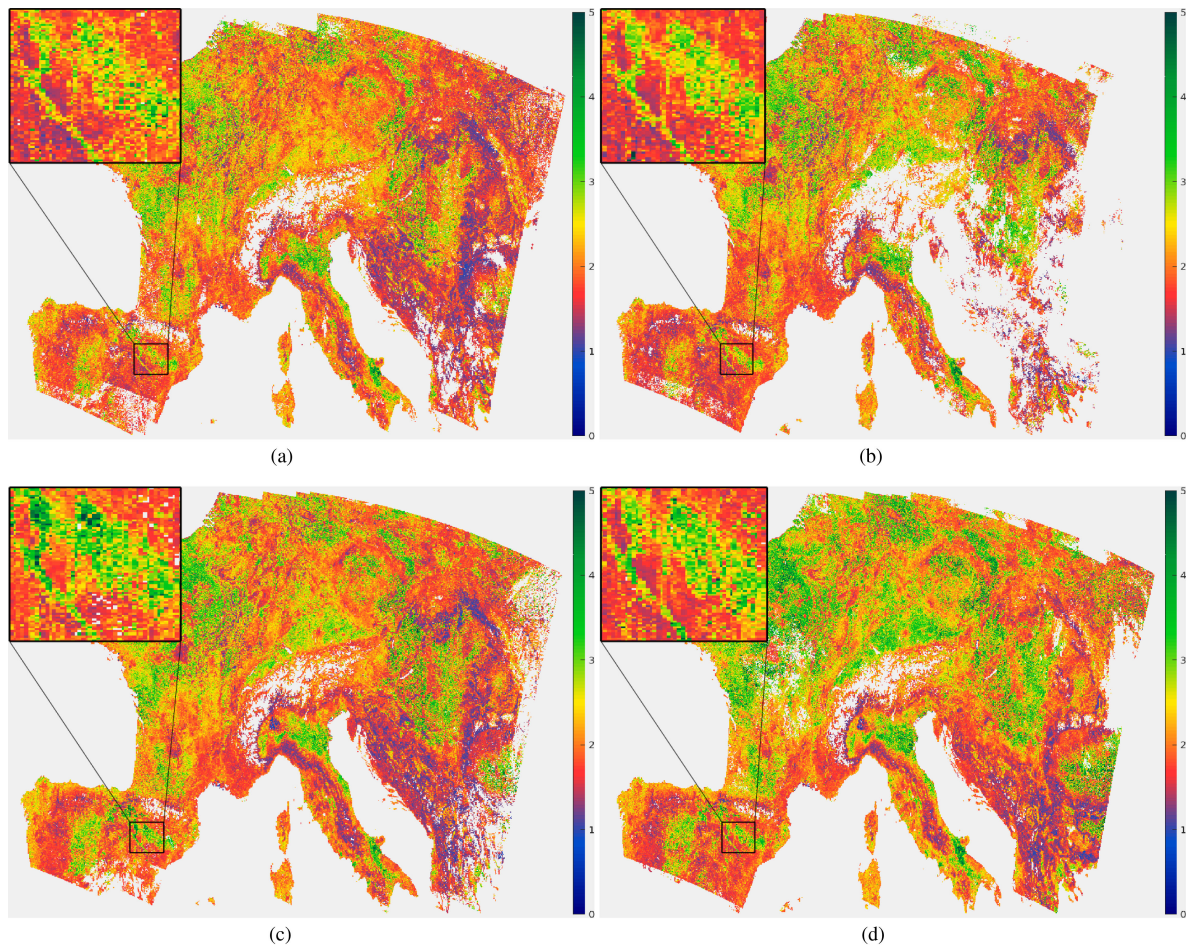


Fig. 9. OTCI mosaics generated by the proposed framework in Experiment 2. Note that the blue to green color scale is used to represent different OTCI values and the gray color expresses unavailable or nonvalid pixels. (a) April-1st. (b) April-2nd. (c) April-3. (d) April-4th.

aspect that deserves to be analyzed in more detail. In particular, Fig. 6 shows the corresponding maps of available observations for the four considered seasonal periods. In this case, the blue to yellow color scale represents the number of valid OTCI values for each dataset, and the gray color expresses unavailable information. Note that each map has a slightly different value range since the maximum number of valid pixels is logically different for each period. Besides, multiple pixel values of Fig. 6(a) are not available due to the high amount of clouds during the winter season. Although we tried to relieve the effect of clouds by considering OTCI products from two weeks, the number of available observations in *Winter-peak* is substantially lower than in the other datasets, being *Spring-peak* and *Summer-peak* the collections with more available information. In general, the number of valid observations within the region of interest tends to be significantly lower than the total number of products considered in each dataset. Precisely, this practical limitation motivates the design of the proposed compositing algorithm and threshold.

It is important to analyze the impact of the available product measurements in operational conditions when generating the corresponding multitemporal mosaics. Therefore, we compare the proposed compositing algorithm (defined within the presented mosaicing framework in Section III-C2) to

different multitemporal compositing alternatives. Specifically, Fig. 7 displays the OTCI composites generated by the proposed approach [see Fig. 7(a)], the mean [see Fig. 7(b)], and the median [see Fig. 7(c)] algorithms using the *Spring-peak* dataset. In addition, Fig. 7 also shows the visual details corresponding to the Spanish natural park *Sierra y Cañones de Guara*. The number of observations in this area is generally below the considered threshold ($th_m = 4$), which helps to better identify potential differences among the compositing alternatives. Note that the proposed approach is able to retrieve higher OTCI values in that location when only few operational product observations are available. Although the straightforward mean and median algorithms tend to reduce the amount of detected chlorophyll in the output composites, the proposed temporal compositing tree algorithm is able to select OTCI values that represent higher pigment levels during the considered temporal period. That is, the defined OLCI-based decision rules are able to discern higher peaks during the spring season when the photosynthetic activity is expected to reach intra-annual maximums in this natural park.

These qualitative results reveal that the proposed approach provides advantages with respect to the mean and median compositing methods, since the combination of the multitemporal OTCI observations is less affected by some product deviations along the periods of interest. In the case of the mean, this one

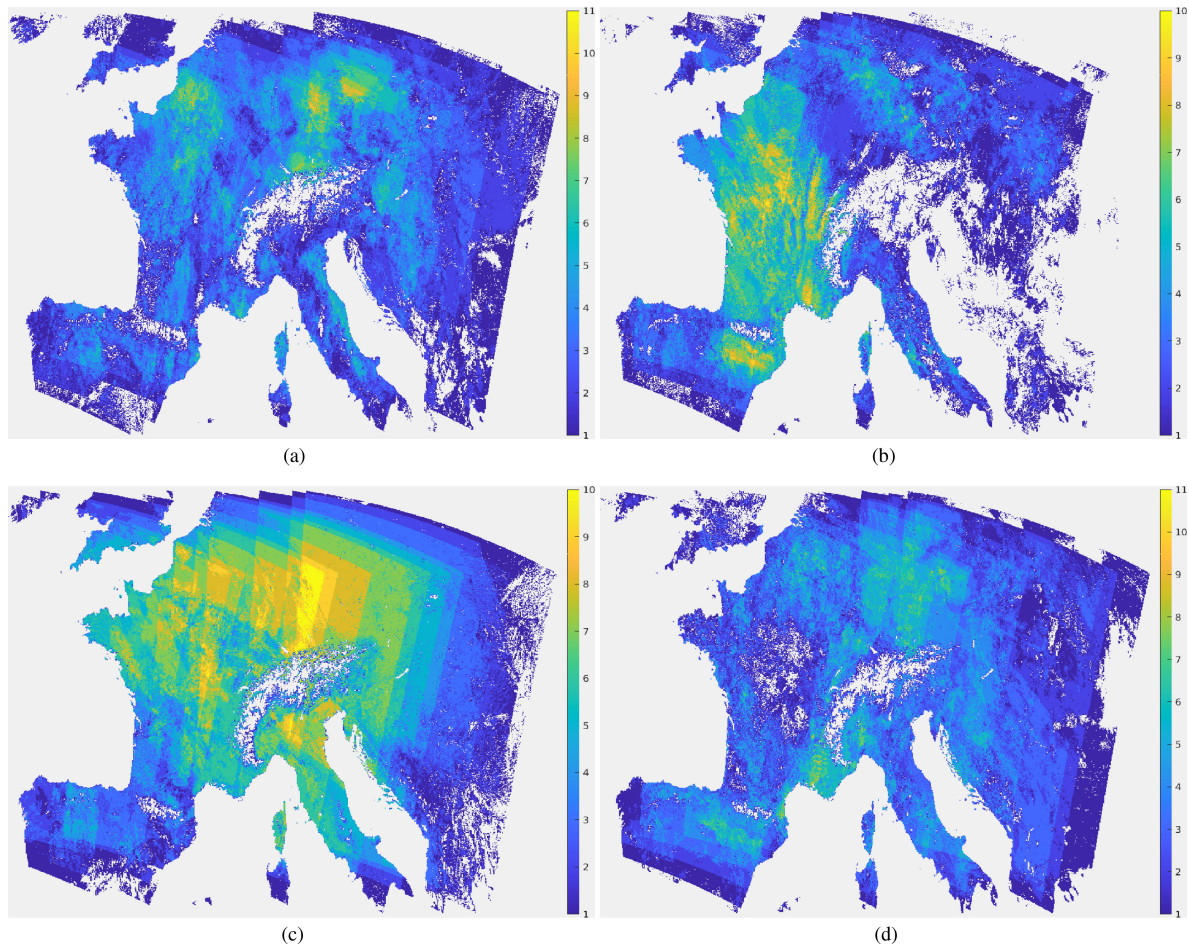


Fig. 10. Valid pixel maps for the OTCI mosaics generated in Experiment 2. Note that the blue to yellow color scale is used to represent valid pixel counts and the gray color expresses unavailable information. (a) April-1st. (b) April-2nd. (c) April-3rd. (d) April-4th.

is the most affected method because it substantially reduces these activation peaks. In the case of the median algorithm, we can see that it logically has a similar behavior to the proposed compositing method when the number of observations is higher than the considered threshold. However, the proposed approach shows better capabilities to combine multitemporal OTCI values while accounting for the natural chlorophyll with limited product observations. Note that both atmospheric contamination effects and temporal limitations are key factors in actual operational environments, where the proposed approach may provide competitive advantages with constrained data.

Finally, Fig. 8 shows the confidence maps for the corresponding OTCI mosaics according to the proposed confidence index (see Section III-D). In this figure, the blue to red color scale represents pixel confidence values and the gray color expresses unavailable information (light gray) or a single valid pixel (dark gray), where the proposed confidence metric is not defined. As it is possible to observe, lower confidence levels do not necessarily correspond with the higher numbers of valid samples in Fig. 6, as some measurements have shown to be rather variable along specific time periods. We can observe different confidence variations depending on the geographic locations and the available observations. For instance, in the case of Fig. 8(d), the north of

France has lower confidence levels than the center of Italy, where more valid temporal OTCI values are available. In general, the confidence values of the generated composites are high with the exception of clouded zones, borders, and some other exceptions. A special mention is deserved by those areas with very few observations. Although the available OTCI measurements are logically correct for this areas, the resulting confidence level is reduced because the product values cannot be contrasted during the temporal period of the mosaic. Note that confidence levels are between 0 and 1, so the map has been scaled according to this interval, with light gray representing unavailable information and dark gray being pixels with less than two valid samples.

2) *Experiment 2*: Regarding the second experiment, Fig. 9 presents the OTCI mosaics generated by the proposed framework for the *April-1st* (a), *April-2nd* (b), *April-3rd* (c), and *April-4th* (d) datasets. Like in the previous experiment, low OTCI values are represented in blue color and green color represents high OTCI measurements. According to the qualitative results reported in Fig. 9, it is possible to see that the weekly mosaics generated for April 2019 have important similarities. However, one can find some noteworthy points according to the expected vegetation grow in the considered area of interest. When analyzing the results from a global perspective, the

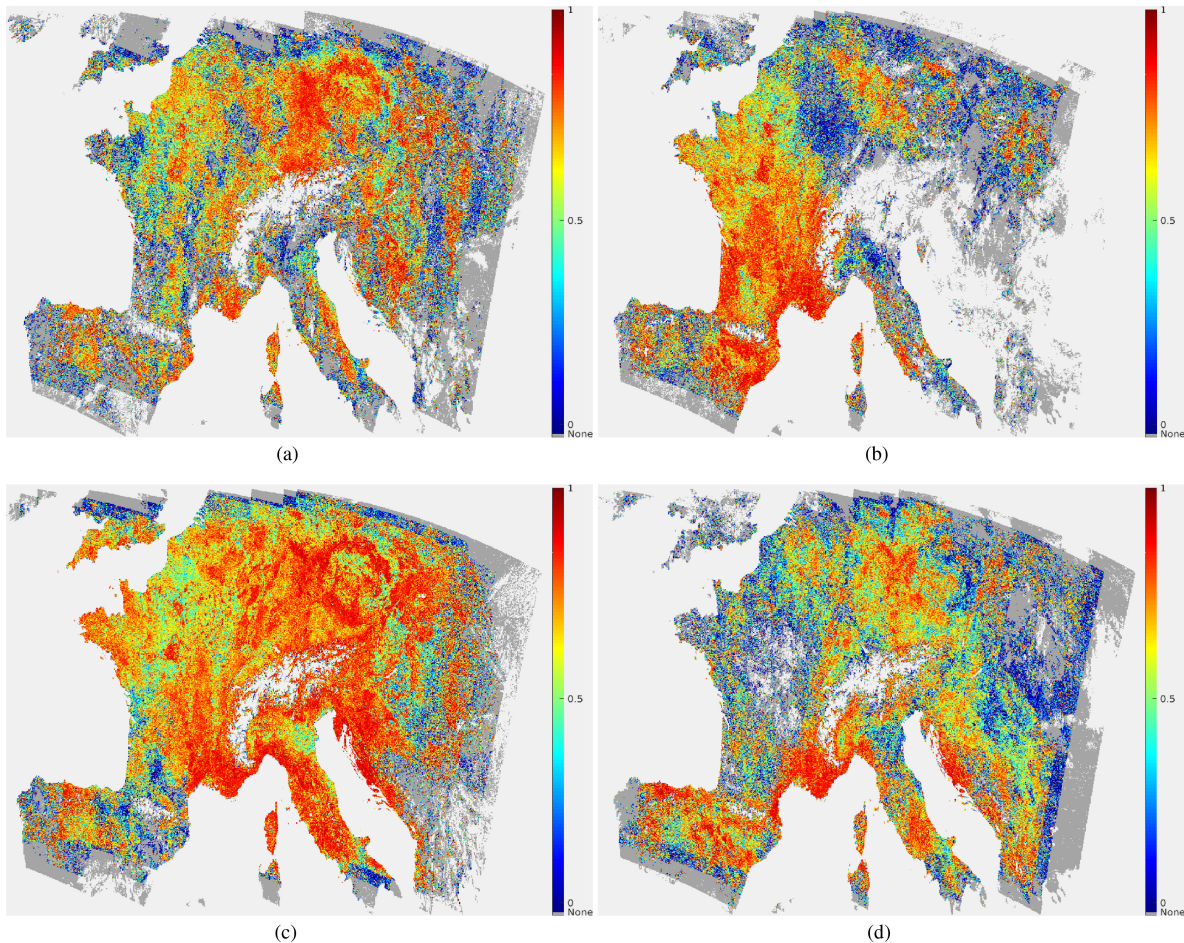


Fig. 11. Confidence maps for the OTCI mosaics generated in Experiment 2. Note that the blue to red color scale is used to represent pixel confidence values and the gray color expresses unavailable information (light gray) or a single valid pixel (dark gray) where the proposed confidence metric is not defined. (a) April-1st. (b) April-2nd. (c) April-3rd. (d) April-4th.

generated multitemporal mosaics reveal that the vegetation in central Europe tends to increase along each week of April, being consistent with the previous interseason analysis, where the maximum amount of green vegetation is reached in the summer season. In the case of the displayed details corresponding to the *Sierra y Cañones de Guara*, we can observe some relevant weekly changes that deserve to be mentioned. Specifically, the highest OTCI activation is achieved in *April-3rd* followed by the *April-4th*, *April-2nd*, and *April-1st* datasets. That is, the peak of the spring season for this natural park can be clearly appreciated in Fig. 9(c), which indicates that the proposed approach is able to generate consistent multitemporal composites that retain the peculiarities of the different regions.

Fig. 10 shows the maps of available observations in Experiment 2. As it is possible to see, there are remarkable differences among the weekly mosaics, since the cloud coverage is typically a very important issue in central Europe during April [47]. The number of valid samples per dataset is generally significantly lower than the total number of available products, with the exception of *April-3rd*. Additionally, Fig. 11 displays the confidence maps of the corresponding OTCI weekly mosaics. As it can be observed, confidence values are higher in those areas with more

valid observations and with a more stable behavior with respect to the amount of vegetation detected by the biophysical index. Note that we follow the same color codes as in Experiment 1 in both figures.

V. CONCLUSION

This work has presented a novel multitemporal mosaicing algorithm specially designed for operational S3 biophysical or other derived products within the context of the S3/FLEX tandem missions. Specifically, the proposed framework has been defined according to four sequential stages/processes (i.e., operational data acquisition, spatial mosaicing, temporal compositing, and confidence level estimation) in order to generate consistent mosaics from derived S3 data products. The conducted experiments, using different S3 datasets, have shown the proposed approach suitability and performance with respect to other standard mosaicing alternatives.

One of the first conclusions that arise from this work is the importance of derived biophysical products within the S3/FLEX context and how generating these multitemporal mosaics can support the operational provision of the missions. On the one

hand, the use of multitemporal data allows significantly reducing the influence of cloud occlusions and contamination due to the high temporal resolution of the instruments. On the other hand, it also enables using substantially wider areas of interest to ease the task of conducting global biophysical analyses. Another important point is related to the operational availability of valid observations and also their inconsistency. The process of selecting a suitable representative pixel value for a given time period is generally very sensitive to the number of valid samples. Unlike standard compositing functions, the proposed approach has been designed to relieve the least informative cases by considering the nature of the derived biophysical product, which may eventually produce more relevant results. Our future work will be focused on the following directions: extending the proposed framework to multimodal RS data, developing empirical models for characterizing FLEX world-wide fluorescence and studying the effect of using different products as well as using in-painting methods for missing data.

REFERENCES

- [1] N. Pettorelli *et al.*, "Satellite remote sensing of ecosystem functions: Opportunities, challenges and way forward," *Remote Sens. Ecol. Conserv.*, vol. 4, no. 2, pp. 71–93, 2018.
- [2] R. Fernandez-Beltran, J. M. Haut, M. E. Paoletti, J. Plaza, A. Plaza, and F. Pla, "Multimodal probabilistic latent semantic analysis for Sentinel-1 and Sentinel-2 image fusion," *IEEE Geosci. Remote Sens. Lett.*, vol. 15, no. 9, pp. 1347–1351, Sep. 2018.
- [3] R. Fernandez-Beltran, P. Latorre-Carmona, and F. Pla, "Single-frame super-resolution in remote sensing: A practical overview," *Int. J. Remote Sens.*, vol. 38, no. 1, pp. 314–354, 2017.
- [4] J. Haas and Y. Ban, "Urban land cover and ecosystem service changes based on Sentinel-2A MSI and Landsat TM data," *IEEE J. Sel. Topics Appl. Earth Observ. Remote Sens.*, vol. 11, no. 2, pp. 485–497, Feb. 2018.
- [5] R. Fernandez-Beltran, J. M. Haut, M. E. Paoletti, J. Plaza, A. Plaza, and F. Pla, "Remote sensing image fusion using hierarchical multimodal probabilistic latent semantic analysis," *IEEE J. Sel. Topics Appl. Earth Observ. Remote Sens.*, vol. 11, no. 12, pp. 4982–4993, Dec. 2018.
- [6] R. Fernandez-Beltran, F. Pla, and A. Plaza, "Sentinel-2 and Sentinel-3 intersensor vegetation estimation via constrained topic modeling," *IEEE Geosci. Remote Sens. Lett.*, vol. 16, no. 10, pp. 1531–1535, Oct. 2019.
- [7] D. Poursanidis and N. Chrysoulakis, "Remote sensing, natural hazards and the contribution of ESA sentinels missions," *Remote Sens. Appl.: Soc. Environ.*, vol. 6, pp. 25–38, 2017.
- [8] L. Zhuo, Q. Dai, D. Han, N. Chen, B. Zhao, and M. Berti, "Evaluation of remotely sensed soil moisture for landslide hazard assessment," *IEEE J. Sel. Topics Appl. Earth Observ. Remote Sens.*, vol. 12, no. 1, pp. 162–173, Jan. 2019.
- [9] R. Fernandez-Beltran, F. Pla, and A. Plaza, "Intersensor remote sensing image registration using multispectral semantic embeddings," *IEEE Geosci. Remote Sens. Lett.*, vol. 16, no. 10, pp. 1545–1549, Oct. 2019.
- [10] R. Fernandez-Beltran, A. Plaza, J. Plaza, and F. Pla, "Hyperspectral unmixing based on dual-depth sparse probabilistic latent semantic analysis," *IEEE Trans. Geosci. Remote Sens.*, vol. 56, no. 11, pp. 6344–6360, Nov. 2018.
- [11] R. Fernandez-Beltran, F. Pla, and A. Plaza, "Endmember extraction from hyperspectral imagery based on probabilistic tensor moments," *IEEE Geosci. Remote Sens. Lett.*, to be published, doi: [10.1109/LGRS.2019.2963114](https://doi.org/10.1109/LGRS.2019.2963114).
- [12] J. Aschbacher and M. P. Milagro-Pérez, "The European Earth monitoring (GMES) programme: Status and perspectives," *Remote Sens. Environ.*, vol. 120, pp. 3–8, 2012.
- [13] M. Berger, J. Moreno, J. A. Johannessen, P. F. Levelt, and R. F. Hanssen, "ESA's Sentinel missions in support of earth system science," *Remote Sens. Environ.*, vol. 120, pp. 84–90, 2012.
- [14] C. Donlon *et al.*, "The Global Monitoring for Environment and Security (GMES) Sentinel-3 mission," *Remote Sens. Environ.*, vol. 120, pp. 37–57, 2012.
- [15] J. Vicent *et al.*, "FLEX end-to-end mission performance simulator," *IEEE Trans. Geosci. Remote Sens.*, vol. 54, no. 7, pp. 4215–4223, Jul. 2016.
- [16] D. Arnas, P. Jurado, I. Barat, B. Duesmann, and R. Bock, "FLEX: A parametric study of its tandem formation with Sentinel-3," *IEEE J. Sel. Topics Appl. Earth Observ. Remote Sens.*, vol. 12, no. 7, pp. 2447–2452, Jul. 2019.
- [17] J. Kravitz, M. Matthews, S. Bernard, and D. Griffith, "Application of sentinel 3 OLCI for chl-a retrieval over small inland water targets: Successes and challenges," *Remote Sens. Environ.*, vol. 237, 2020, Art. no. 111562.
- [18] D. Kyrilyuk and S. Kratzer, "Evaluation of Sentinel-3A OLCI products derived using the case-2 regional coastcolour processor over the baltic sea," *Sensors*, vol. 19, no. 16, 2019, Art. no. 3609.
- [19] L. A. Brown, J. Dash, A. L. Lidón, E. Lopez-Baeza, and S. Dransfeld, "Synergetic exploitation of the Sentinel-2 missions for validating the Sentinel-3 ocean and land color instrument terrestrial chlorophyll index over a vineyard dominated mediterranean environment," *IEEE J. Sel. Topics Appl. Earth Observ. Remote Sens.*, vol. 12, no. 7, pp. 2244–2251, Jul. 2019.
- [20] A. Kokhanovsky *et al.*, "Retrieval of snow properties from the Sentinel-3 ocean and land colour instrument," *Remote Sens.*, vol. 11, no. 19, 2019, Art. no. 2280.
- [21] Z. Zhang, L. Zhao, and A. Lin, "Evaluating the performance of Sentinel-3A OLCI land products for gross primary productivity estimation using ameriflux data," *Remote Sens.*, vol. 12, no. 12, 2020, Art. no. 1927.
- [22] H. Lyu *et al.*, "A novel algorithm to estimate phytoplankton carbon concentration in inland lakes using Sentinel-3 OLCI images," *IEEE Trans. Geosci. Remote Sens.*, vol. 58, no. 9, pp. 6512–6523, Sep. 2020.
- [23] P. Team, "GMES space component sentinel-3 payload data ground segment products definition document," Eur. Space Agency, Paris, France, Tech. Rep. GMES-S3GS-EOPG-TN-12-0004, Nov. 2016.
- [24] Z. Xiao, "Compositing, smoothing, and gap-filling techniques," in *Adv. Remote Sens., Terr. Inf. Extraction and Appl.* New York, NY, USA: Academic, 2012, pp. 75–90.
- [25] Y. Guo, F. Li, P. A. Caccetta, and D. Devereux, "Multiple temporal mosaicking for Landsat satellite images," *J. Appl. Remote Sens.*, vol. 11, no. 1, 2017, Art. no. 015021.
- [26] B. N. Holben, "Characteristics of maximum-value composite images from temporal AVHRR data," *Int. J. Remote Sens.*, vol. 7, no. 11, pp. 1417–1434, 1986.
- [27] J. Cihlar, D. Manak, and M. D'Iorio, "Evaluation of compositing algorithms for AVHRR data over land," *IEEE Trans. Geosci. Remote Sens.*, vol. 32, no. 2, pp. 427–437, Mar. 1994.
- [28] A. Huete, K. Didan, T. Miura, E. P. Rodriguez, X. Gao, and L. G. Ferreira, "Overview of the radiometric and biophysical performance of the modis vegetation indices," *Remote Sens. Environ.*, vol. 83, nos. 1/2, pp. 195–213, 2002.
- [29] D. P. Roy *et al.*, "Web-enabled Landsat Data (WELD): Landsat ETM+ composited mosaics of the conterminous United States," *Remote Sens. Environ.*, vol. 114, no. 1, pp. 35–49, 2010.
- [30] P. Potapov, S. Turubanova, and M. C. Hansen, "Regional-scale boreal forest cover and change mapping using landsat data composites for European Russia," *Remote Sens. Environ.*, vol. 115, no. 2, pp. 548–561, 2011.
- [31] V. Kovalsky and D. P. Roy, "The global availability of Landsat 5 TM and Landsat 7 ETM+ land surface observations and implications for global 30 m landsat data product generation," *Remote Sens. Environ.*, vol. 130, pp. 280–293, 2013.
- [32] Sen2Three: Sentinel-2 level 3 spatio-temporal synthesis processor, Version 1.0.0. Documentation, 2017. Accessed: Apr. 1, 2020. [Online]. Available: <https://step.esa.int/thirdparties/sen2three/1.0.0/>
- [33] The Sentinel-2 global mosaic service, 2018. Accessed: Apr. 1, 2020. [Online]. Available: <https://land.copernicus.eu/imagery-in-situ/global-image-mosaics/>
- [34] G. Schmidt, C. B. Jenkerson, J. Masek, E. Vermote, and F. Gao, "Landsat ecosystem disturbance adaptive processing system (LEDAPS) algorithm description," U.S. Geol. Survey, Reston, VA, USA, Tech. Rep. 2013-1057, 2013.
- [35] P. V. Potapov *et al.*, "Quantifying forest cover loss in Democratic Republic of The Congo, 2000–2010, with Landsat ETM+ data," *Remote Sens. Environ.*, vol. 122, pp. 106–116, 2012.
- [36] M. C. Hansen, D. P. Roy, E. Lindquist, B. Adusei, C. O. Justice, and A. Altstatt, "A method for integrating modis and Landsat data for systematic monitoring of forest cover and change in the congo basin," *Remote Sens. Environ.*, vol. 112, no. 5, pp. 2495–2513, 2008.
- [37] N. Flood, "Seasonal composite Landsat TM/ETM+ images using the medoid (a multi-dimensional median)," *Remote Sens.*, vol. 5, no. 12, pp. 6481–6500, 2013.

- [38] A. Struyf, M. Hubert, and P. Rousseeuw, "Clustering in an object-oriented environment," *J. Statist. Softw.*, vol. 1, no. 4, pp. 1–30, 1997.
- [39] J. Louis *et al.*, "Sentinel-2 Sen2COR: L2A processor for users," in *Proc. Living Planet Symp.*, 2016, pp. 1–8.
- [40] Sentinel application platform (SNAP), 2017. Accessed: Apr. 21, 2020. [Online]. Available: <https://step.esa.int/main/toolboxes/snap/>
- [41] Y. Cheng, K. Zhou, J. Wang, and J. Yan, "Big earth observation data integration in remote sensing based on a distributed spatial framework," *Remote Sens.*, vol. 12, no. 6, 2020, Art. no. 972.
- [42] Copernicus open access hub, 2017. Accessed: Apr. 21, 2020. [Online]. Available: <https://scihub.copernicus.eu/>
- [43] "Ocean and land colour instrument (OLCI) algorithm theoretical basis document, 2010. Accessed: May. 19, 2020. [Online]. Available: https://sentinels.copernicus.eu/documents/247904/349589/OLCI_L2_ATBD_FA%PAR.pdf
- [44] X. Wang and C. S. Zender, "MODIS snow albedo bias at high solar zenith angles relative to theory and to *in situ* observations in greenland," *Remote Sens. Environ.*, vol. 114, no. 3, pp. 563–575, 2010.
- [45] High-resolution landcover CCI project, 2018. Accessed: Apr. 12, 2020. [Online]. Available: <http://cci.esa.int/hlandcover/>
- [46] Student, "The probable error of a mean," *Biometrika*, vol. 6, pp. 1–25, 1908.
- [47] R. Stöckli and P. L. Vidale, "European plant phenology and climate as seen in a 20-year AVHRR land-surface parameter dataset," *Int. J. Remote Sens.*, vol. 25, no. 17, pp. 3303–3330, 2004.
- [48] M. Palahi, M. Tomé, T. Pukkala, A. Trasobares, and G. Montero, "Site index model for *Pinus sylvestris* in north-east Spain," *Forest Ecol. Manag.*, vol. 187, no. 1, pp. 35–47, 2004.
- [49] J. Riedel, A. Bernues, and I. Casasus, "Livestock grazing impacts on herbage and shrub dynamics in a mediterranean natural park," *Rangeland Ecol. Manag.*, vol. 66, no. 2, pp. 224–233, 2013.
- [50] A. Trasobares, T. Pukkala, and J. Miina, "Growth and yield model for uneven-aged mixtures of *Pinus sylvestris* L. and *Pinus nigra* Arn. in Catalonia, north-east Spain," *Ann. Forest Sci.*, vol. 61, no. 1, pp. 9–24, 2004.



Damian Ibañez received the B.S. degree in industrial electronics and automation engineering from the Polytechnic University of Valencia, Valencia, Spain, in 2019. He is currently working toward the M.S. degree in intelligent systems with Universitat Jaume I, Castellón de la Plana, Spain.

His research interests include computer vision and machine learning, with special interest in remote sensing applications.



Ruben Fernandez-Beltran (Senior Member, IEEE) received the B.Sc. degree in computer science, the M.Sc. degree in intelligent systems, and the Ph.D. degree in computer science from Universitat Jaume I, Castellón de la Plana, Spain, in 2007, 2011, and 2016, respectively.

He was a Visiting Researcher with the University of Bristol, Bristol, U.K., the University of Cáceres, Cáceres, Spain, and the Technische Universität Berlin, Berlin, Germany. He is currently a Postdoctoral Researcher with the Computer Vision

Group, Universitat Jaume I, where he is also a member of the Institute of New Imaging Technologies. His research interests include multimedia retrieval, spatio-spectral image analysis, pattern recognition techniques applied to image processing, and remote sensing.

Dr. Fernandez-Beltran received the Outstanding Ph.D. Dissertation Award at Universitat Jaume I, in 2017. He is a member of the Spanish Association for Pattern Recognition and Image Analysis, which is part of the International Association for Pattern Recognition.



José Martínez Sotoca received the B.Sc. degree in physics from the Universidad Nacional de Educación a Distancia, Madrid, Spain, in 1996, and the M.Sc. and Ph.D. degrees in physics from the University of Valencia, Valencia, Spain, in 1999 and 2001, respectively.

His Ph.D. work was on surface reconstructions with structured light. He is currently an Assistant Lecturer with the Departamento de Lenguajes y Sistemas Informáticos, Universitat Jaume I, Castellón de la Plana, Spain.

He has authored or coauthored more than 100 scientific papers in national and international conference proceedings, books, and journals. His research interests include pattern recognition and biomedical applications, including image pattern recognition, hyperspectral data, structured light, and feature extraction and selection.



Ramón A. Mollineda received the Ph.D. degree in computer science from the Polytechnic University of Valencia, Valencia, Spain, in 2001.

He is currently an Associate Professor with the Department of Computer Languages and Systems, Universitat Jaume I, Castellón de la Plana, Spain. His research interests include machine learning, computer vision, biomedical signals, and gait analysis.

Dr. Mollineda is a member of the Spanish Association for Pattern Recognition and Image Analysis and the International Association for Pattern Recognition.



José Moreno (Senior Member, IEEE) received the M.Sc. degree in physics and the Ph.D. degree in theoretical physics from the University of Valencia, Valencia, Spain, in 1986 and 1992, respectively. He is a Full Professor of Earth Physics with the Department of Earth Physics and Thermodynamics, Faculty of Physics, University of Valencia, Valencia, Spain. He teaches and works on different projects related to remote sensing and space research as director of the Laboratory for Earth Observation, Image Processing Laboratory/Scientific Park, University of Valencia.

He has been involved in many international projects and research networks. He was also involved in the preparatory activities and exploitation programs of several satellite missions, such as ENVISAT, CHRIS/PROBA, Copernicus/Sentinels 1-2-3, SEOSAT/Ingenio. He is the Principal Investigator and Chair of the Mission Advisory Group of the Fluorescence Explorer, Earth Explorer Mission of the European Space Agency (ESA). His research interests include the modeling and monitoring of land surface processes by using remote sensing techniques.

Prof. Moreno was a member of the ESA Earth Sciences Advisory Committee, the International Space Station Users Panel, and other international advisory committees. He was General Chair of the 2018 IEEE International Geoscience and Remote Sensing Symposium, has served as the Guest Editor for the IEEE JOURNAL OF SELECTED TOPICS IN APPLIED EARTH OBSERVATIONS AND REMOTE SENSING. He is an Associate Editor for the IEEE TRANSACTIONS ON GEOSCIENCE AND REMOTE SENSING.



Filiberto Pla received the B.Sc. and Ph.D. degrees in physics from the Universitat de València, València, Spain, in 1989 and 1993, respectively.

He is currently a Full Professor with the Department de Llenguatges i Sistemes Informàtics, Universitat Jaume I, Castellón de la Plana, Spain. He has been a Visiting Scientist with the Silsoe Research Institute, the University of Surrey, the University of Bristol in U.K., CEMAGREF in France, the University of Genoa in Italy, the Instituto Superior Técnico of Lisbon in Portugal, the Swiss Federal Institute of

Technology Zurich, the Idiap Research Institute in Switzerland, the Technical University of Delft, The Netherlands, and the Mid Sweden University in Sweden. He is the Director of the Institute of New Imaging Technologies, Universitat Jaume I. His current research interests include color and spectral image analysis, visual motion analysis, 3-D image visualization, and pattern recognition techniques applied to image processing.

Dr. Pla is a member of the Spanish Association for Pattern Recognition and Image Analysis, which is part of the International Association for Pattern Recognition.